Learning glioblastoma immune phenotypes from 3D whole-brain MRI

Anonymous Authors[1]

Anonymous Institution
anonymous@domain.com

Abstract. Glioblastoma exhibits profound heterogeneity in its immune microenvironment, limiting the clinical utility of tissue-based immune profiling and hindering patient stratification for immunotherapy. Existing imaging biomarkers typically rely on region-of-interest radiomics or single-cohort training, restricting their generalizability across institutions and acquisition protocols. In this study, we introduce DECIPHER-GBM, a hybrid autoencoder-classifier framework that learns immune phenotypes directly from 3D whole-brain MRI and has been evaluated under cross-cohort domain shift. By integrating latent space representations with transcriptomics-derived immune labels, we demonstrate that global tumor-associated macrophage burden can be inferred non-invasively across three independent datasets (mean precision 0.74, balanced accuracy 0.70, MCC 0.11). Probabilistic and calibration analyses reveal phenotype-specific uncertainty patterns that align with known glioblastoma biology. This work establishes a scalable and interpretable imaging-based approach for immune phenotyping in glioblastoma, providing a foundation for prospective validation and future integration into adaptive trial design and treatment stratification.

Keywords: radiogenomics · autoencoder · immunotherapy · glioblastoma.

1 Introduction

Standard-of-care treatment for IDH-wildtype (wt) glioblastoma remains limited, with median survival of approximately 15–18 months, largely due to intratumoral heterogeneity and an immunosuppressive tumor microenvironment (TME) [27,17,10,7]. Neo-adjuvant immunotherapy trials in recurrent glioblastoma have demonstrated enhanced anti-tumor immune activation, including upregulation of cytotoxic immune gene programs and suppression of proliferative pathways [9,22], with similar interferon-driven immune activation and tumor cell-cycle downregulation now reported in newly diagnosed disease [21], leading to ongoing clinical trial evaluation [8]. Within the TME, tumor-associated macrophages (TAMs) are key regulators of immune suppression, invasion, and angiogenesis [10,7], with macrophage abundance and activation states strongly associated

with progression and treatment resistance, positioning TAMs as a major therapeutic target, albeit constrained by spatial heterogeneity and dynamic immune states [6,18,29].

Radiogenomics offers a potential non-invasive route to characterise these immune states [11], but most existing approaches rely on segmented tumor radiomics within single cohorts, limiting interpretability and generalisability [8,6,11,24]. In addition, immune phenotypes derived from bulk transcriptomic deconvolution are continuous and overlapping biological states that are often binarised using arbitrary thresholds, failing to capture inherent uncertainty [16,28,13,14]. Deep learning approaches using whole-brain MRI provide an alternative by learning latent representations that capture global tumor and microenvironment context without explicit tumor segmentation [1,26]. Autoencoder-based frameworks enable unsupervised representation learning with compact latent spaces suitable for downstream prediction tasks [1,26,23]. When combined with probabilistic outputs and cross-cohort validation, these methods offer a scalable approach for immune phenotyping and potential clinical trial enrichment strategies, including pre-trial biopsy selection and stratification of inoperable or deep-seated lesions [3].

Here, we present DECIPHER-GBM, a hybrid 3D autoencoder-classifier framework for non-invasive immune phenotyping of IDH-wt glioblastoma using 3D whole-brain MRI.

2 Methods

We performed a retrospective multi-center validation study using international open-access IDH-wt glioblastoma multimodal (imaging and genomic) data.

2.1 Matched data and cross-cohort strategy

We assembled matched 3D multi-sequence brain MRI data from five open-access cohorts together with 17 deconvolution-derived patient-level immune signatures using pan-cancer and glioblastoma-specific reference libraries. Imaging included T1, T1CE, T2, and FLAIR sequences. A cross-cohort training strategy [12] was implemented using three complementary dataset splits to assess robustness under domain shift. Group 1 was trained on CGGA, TCGA-GBM, CPTAC, and REMBRANDT, with IvyGAP held out for testing; Group 2 held out TCGA-GBM; and Group 3 held out CPTAC. For each split, training and validation sets were derived using a 9:1 random partition. CGGA and REMBRANDT were used exclusively in training to preserve evaluation integrity, with CGGA supplemented by synthetic FLAIR due to missing sequences and REMBRANDT contributing microarray-based profiles; both were excluded from testing to avoid bias. This design ensured evaluation on fully unseen cohorts while maintaining heterogeneous training exposure. Reporting followed CLAIM and TRIPOD-AI guidelines.

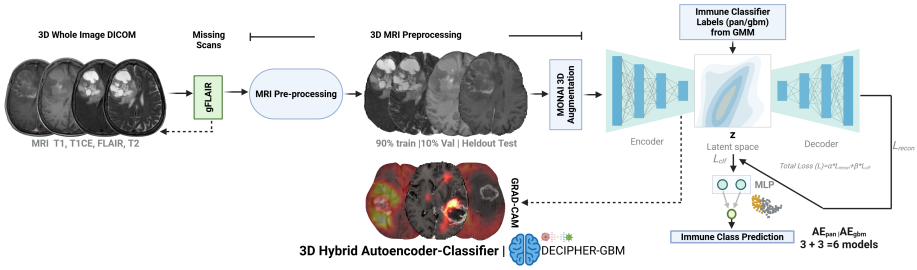

Fig. 1: DECIPHER-GBM architecture. Preprocessed and augmented 3D MRI images were passed through a 3D hybrid autoencoder-classifier architecture to produce immune class predictions based on the binary immune classifier labels. Grad-CAM explainability images were generated from the final encoder layer before the latent space.

2.2 Gaussian mixture model-based outcome definition

Immune phenotype outcomes were defined using transcriptomic−derived continuous scores obtained from harmonized bulk deconvolution of tumor tissue transcriptomics using CIBERSORTx. Each immune score distribution was modelled using a two-component Gaussian mixture model (GMM), representing low and high immune states, rather than applying arbitrary thresholds. Samples were assigned to high or low immune classes based on posterior boundary inference.

2.3 MRI preprocessing

We included all four MRI sequences in preprocessing. The multi-institutional dataset exhibited heterogeneity in field strength (1.5T, 3T, unknown), scanner vendor (GE, Siemens, Philips, unknown), and acquisition era (1980s–2000s). DICOM images were converted to NIfTI format using SimpleITK. Synthetic FLAIR images were generated to compensate for missing sequences in 66/176 CGGA cases using two approaches: the in-house PRECISE_GAN pipeline and BraTS orchestrator synthetic imaging pipeline. Preprocessing was performed using the BrainLesion Suite (Fig. 1), including N4 bias field correction, followed by co-registration to T1CE and atlas registration using ANTs. Subsequent steps included skull stripping, intensity normalization, resampling to a 128×128×128 grid, and per-volume min–max scaling to [0,1].

2.4 Network architecture

We used a 3D convolutional autoencoder (AE) with an MLP classification head on the latent representation (Fig. 1). The encoder consisted of four convolutional blocks with channel depths of 32, 64, 128, and 256, followed by flattening and a fully connected projection to a latent vector $z \in \mathbb{R}^{256}$. A sigmoid activation constrained reconstructed intensities to $[0, 1]$ after intensity normalization. For

immune phenotype prediction, the latent vector was fed into an MLP classifier (256→128 with ReLU), followed by dropout (0.3) and a final linear layer producing a binary logit. The AE learned a label-independent latent representation of whole-brain MRI, while the classifier mapped latent features to GMM-defined immune states via a probabilistic projection rather than enforcing the GMM boundary in latent space. This joint architecture enabled simultaneous optimisation of reconstruction fidelity and immune-relevant feature learning while preserving anatomically meaningful latent structure.

2.5 Training objective and optimization

Each batch optimizes a joint objective (Total loss L) combining reconstruction and classification:

$$L = \alpha * L_r econ + \beta * L_c lf$$

The two losses were reconstruction loss ($L_r econ$) (obtained from mean-squared error (MSE) between input and reconstruction on the full input tensor) and classification loss ($L_c lf$) (obtained from binary cross-entropy (BCE) with logits). Hyperparameters were fixed across all experiments : $\alpha = 0.3; \beta = 0.7$, AdamW optimizer with $LR = 10e - 5$ and $weightdecay = 10e - 4$, $batchsize = 1$, $epochs = 300$, $latentsize = 256$.

2.6 Data augmentation

Three-dimensional data augmentation of random axis-aligned flips, random intensity scaling and random contrast adjustment were applied during training using the MONAI framework to improve robustness to spatial and intensity variability across multi-institutional MRI datasets.

2.7 Model training and selection

Six training regimes were evaluated, each producing a single final model selected by validation performance. Primary selection was based on mean balanced accuracy (BA) across immune labels, with mean precision used as a tie-breaker. All models were trained for up to 300 epochs and early stopping was applied when divergence between decreasing training loss and increasing validation loss indicated overfitting; the best validation checkpoint was retained. We evaluated two immune reference libraries (pan-cancer and glioblastoma signature matrices) across three cross-cohort training designs with distinct held-out test sets (IvyGAP, TCGA-GBM, CPTAC), resulting in six independently trained models (three AE_{pan} and three AE_{gbm}).

2.8 Explainability using Grad-CAM

To interpret the spatial features contributing to immune phenotype predictions, gradient-weighted class activation mapping (Grad-CAM) was applied to the

trained models. Grad-CAM maps were generated from the final convolutional layer of the encoder, prior to the latent space bottleneck, as this layer preserves high-level spatial representations while retaining anatomical signals. The maps were normalized and overlaid on TI CE images for visualization.

2.9 Statistical analysis

All analyses were performed on held-out cohorts within a cross-cohort evaluation framework. Model performance was independently assessed across three test cohorts. Bootstrap resampling (10,000 iterations) was used to estimate empirical metric distributions and 95% confidence intervals (CIs). Pairwise AE_{pan} vs AE_{gbm} comparisons were considered significant when CIs excluded zero after Bonferroni correction. Calibration was evaluated using Brier score, expected calibration error (ECE), and maximum calibration error (MCE). Class probabilities were derived from sigmoid outputs of best-performing models, and density estimates at a 0.5 threshold were used to characterise error distributions. Prediction confidence was stratified by calibrated posterior scores: ≥ 0.80 (high label-dominant), 0.60–0.79 (moderate label-dominant), 0.40–0.59 (low confidence boundary), 0.20–0.39 (moderate label-low), and < 0.20 (high label-low).

3 Results

A total of 176 IDH-wt glioblastoma patients with matched transcriptomic and imaging data were included. No significant differences in overall survival (OS) were observed across datasets or when grouped into three cohorts, across age, gender, OS, or tumour volume. The BraTS Orchestrator synthetic image pipeline produced the most stable synthetic images and was used to generate gFLAIR images.

Six models from two signature matrix reference standards (AE_{pan}, AE_{gbm}) were trained, validated, and tested across three held-out cohorts (Groups 1–3). Five immune labels were shared across both standards: immune score, T cells, tumor-associated macrophages (TAMs), dendritic cells (DCs), and natural killer (NK) cells.

3.1 Held-out test cohort performance

Test performance ranges for AE_{pan} were BA: 0.53–0.62, accuracy: 0.57–0.71, precision: 0.42–0.56, and MCC: -0.01–0.06, and for AE_{gbm} were BA: 0.55–0.96, accuracy: 0.74–0.96, precision: 0.29–0.42, and MCC: -0.09–0.04 (Fig. 2b). A general reduction in MCC was observed in test cohorts compared with validation, indicating reduced generalisation under distribution shift.Under class imbalance, only weak immune discrimination was observed, with low MCC values in CPTAC for AE_{gbm} (0.04) and TCGA-GBM for AE_{pan} (0.06). Performance in IvyGAP remained challenging across models (AE_{gbm}: -0.09; AE_{pan}: 0.01), likely reflecting small sample size (n=16) and severe class imbalance. Detailed results per metric,

Table 1: Performance of AE_{pan} and AE_{gbm} models. Values are reported as mean (range). BA = balanced accuracy; MCC = Matthews correlation coefficient; IS = immune score; DCs = dendritic cells; Tregs = regulatory T cells; M0/M1/M2 Mac = M0/M1/M2 macrophages; TAMs = tumour-associated macrophages; NK = natural killer.

Reference standard	Category	BA	Precision	MCC
(AE_{pan}, Groups 1–3)				
	IS	0.73 (0.50–1.00)	0.89 (0.67–1.00)	0.00 (0.00–0.00)
	CD4 T*	0.63 (0.44–0.96)	0.42 (0.00–1.00)	−0.04 (−0.12–0.00)
	CD8 T	0.51 (0.40–0.64)	0.59 (0.44–0.77)	−0.006 (−0.29–0.28)
	Tregs*	0.44 (0.40–0.50)	0.25 (0.00–0.74)	−0.13 (−0.22–0.00)
	T cells*	0.38 (0.00–0.67)	0.45 (0.00–0.91)	0.08 (−0.08–0.32)
	M1 Mac*	0.65 (0.46–1.00)	0.00 (0.00–0.00)	0.00 (0.00–0.00)
	M2 Mac	0.52 (0.38–0.67)	0.51 (0.25–1.00)	0.00 (−0.23–0.23)
	M0 Mac	0.68 (0.50–0.85)	0.90 (0.69–1.00)	0.00 (0.00–0.00)
	TAMs	0.68 (0.52–0.80)	0.58 (0.25–1.00)	0.29 (0.10–0.40)
	DCs	0.70 (0.50–0.80)	0.92 (0.88–1.00)	0.05 (−0.18–0.32)
	NK*	0.67 (0.50–1.00)	0.00 (0.00–0.00)	0.00 (0.00–0.00)
(AE_{gbm}, Groups 1–3)				
	IS	0.97 (0.92–1.00)	1.00 (1.00–1.00)	0.00 (0.00–0.00)
	T cells*	0.81 (0.50–0.96)	0.00 (0.00–0.00)	0.00 (0.00–0.00)
	TAMs	0.71 (0.42–0.96)	0.90 (0.71–1.00)	−0.07 (−0.21–0.00)
	Microglia*	0.83 (0.50–1.00)	0.00 (0.00–0.00)	0.00 (0.00–0.00)
	DCs*	0.78 (0.43–0.96)	0.00 (0.00–0.00)	−0.05 (−0.14–0.00)
	NK*	0.64 (0.46–0.89)	0.17 (0.00–0.50)	0.02 (−0.15–0.22)
Pooled results (AE_{gbm} + AE_{pan})				
	Score	0.85 (0.50–1.00)	0.95 (0.67–1.00)	0.00 (0.00–0.00)
	TAMs	0.70 (0.42–0.96)	0.74 (0.25–1.00)	0.11 (−0.21–0.40)

* categories with marked class imbalance leading to metric collapse and undefined results.

model, and immune category are summarised in Table 1. Only immune score and TAMs were consistently evaluable across all six models without metric collapse. TAMs showed the most stable signal across cohorts, with pooled performance (AE_{gbm} + AE_{pan}) yielding BA 0.70 (0.42–0.96), precision 0.74 (0.25–1.00), and MCC 0.11 (−0.21–0.40), suggesting a detectable radiogenomic signal.

3.2 Bootstrap post hoc analysis

Bootstrap resampling showed that AE_{gbm} achieved higher BA than AE_{pan} in TCGA-GBM (mean difference 0.33, 95% CI 0.16–0.44) and CPTAC (0.29, 0.02–0.56), whereas AE_{pan} outperformed AE_{gbm} in IvyGAP (-0.27, -0.45 to -0.12). Confidence intervals indicated significant BA differences across all cohorts; however, after Bonferroni correction, only TCGA-GBM and IvyGAP remained significant. Differences in precision and MCC were inconsistent and not significant after correction, likely reflecting class imbalance and cohort-specific prevalence.

3.3 Calibration performance across cohorts for TAMs models

For TAMs, AE_{gbm} showed low–moderate Brier scores (0.03, 0.20, 0.33), ECE (0.09, 0.28, 0.32), and MCE (0.62, 0.96, 0.92) across TCGA-GBM, CPTAC, and IvyGAP, respectively, indicating good calibration in TCGA-GBM but reduced accuracy across external cohorts, likely reflecting small sample size and

class imbalance, particularly in IvyGAP. Site-specific calibration is therefore recommended for downstream radiogenomic inference. In contrast, AE_{pan} demonstrated consistent miscalibration, with Brier scores (0.67, 0.34, 0.26), ECE (0.71, 0.41, 0.32), and MCE (0.75, 0.83, 0.80), most evident in TCGA-GBM, resulting in under-confidence for TAMs-high cases and higher false-negative rates, limiting its standalone downstream utility.

3.4 Probability analysis of TAMs model predictions

TAMs predictions showed heterogeneous probability distributions across held-out cohorts for both AE_{pan} and AE_{gbm}, indicating that local probability calibration, particularly for AE_{gbm}, may improve radiogenomic signal extraction. AE_{gbm} correctly identified TAMs-high cases in CPTAC (19/25, 76%; 78.9% high-, 5.3% moderate-, 15.7% low-confidence), TCGA-GBM (26/27, 96.3%; 84.6% high-, 11.5% moderate-, 3.9% low-confidence), and IvyGAP (10/16, 62.5%; all high-confidence). In contrast, AE_{pan} correctly identified TAMs-low cases in CPTAC (13/25, 52%; 76.9% high/moderate- and 23.1% low-confidence), TCGA-GBM (6/27, 23.1%; all high-confidence), and IvyGAP (7/16, 43.8%; 42.9% high- and 57.1% moderate-confidence). Overall, AE_{gbm} demonstrated greater sensitivity for TAMs-high detection, whereas AE_{pan} showed a more conservative classification pattern with higher false-negative rates.

3.5 Grad-CAM results

Grad-CAM heatmaps demonstrated a reproducible pattern for TAMs prediction. High-confidence TAMs-high cases predicted by the AE_{gbm} model showed prominent saliency in ventricular-periventricular regions whereas TAMs-low cases by AE_{pan} model showed more diffuse parenchymal or peripheral heatmap activations. Low to moderate confidence cases showed mixed patterns. These activations indicated informative regions for the model's decision supporting plausibility of extracting TAMs signal from whole-brain MRI images.

4 Discussion

The DECIPHER-GBM study shows that immune phenotyping in IDH-wildtype glioblastoma can be inferred from whole-brain MRI using a deep learning framework, with TAMs emerging as a generalisable non-invasive imaging biomarker across heterogeneous cohorts. The matched dataset is one of the largest open-access IDH-wt GBM cohorts under WHO 2021 classification, integrating imaging and transcriptomic data while reducing sampling bias. This framework extends prior radiogenomic work [11,19,15,20,5,4,12] through key design differences. First, it uses whole 3D MRI volumes rather than tumour-only segmentation, capturing global anatomical context relevant to immune states. Second, it employs a hybrid autoencoder-classifier architecture instead of conventional models [11,12] or purely discriminative deep learning [2,25], enabling

reconstruction-driven latent learning that preserves anatomical structure while supporting immune classification. Third, MONAI-based 3D augmentation introduces controlled variability, improving robustness under domain shift and reducing overfitting.

Additionally, probabilistic outputs and calibration analyses show stable TAMs predictions across cohorts and transcriptomic standards, while Grad-CAM indicates spatially coherent saliency. The multi-label formulation with shared latent representations captures tumour microenvironment complexity, enabling modelling of interacting immune phenotypes rather than independent decision boundaries.

5 Limitations

Four limitations are identified. First, glioblastoma heterogeneity limits spatial resolution; whole-brain modelling captures global context but not fine infiltrative immune variation, creating a trade-off between robustness and specificity. Second, immune labels derived from bulk transcriptomic deconvolution act as pseudo-labels, and platform differences (microarray vs RNA-seq) introduce noise, compounded by deconvolution assumptions. Lack of immunohistochemistry validation further limits biological ground truth, while TCGA/CPTAC provide tumour-level averages and IvyGAP region-specific states, creating cross-cohort scale mismatch. Third, limited sample sizes and class imbalance affect metric stability, particularly for TAMs-low, and although external validation was performed, the study remains retrospective and requires prospective validation. Fourth, interpretability remains partial: while Grad-CAM provides saliency maps, it does not imply causality, and predictions should be interpreted as probabilistic estimates of immune state.

6 Conclusion

This study demonstrates that whole-brain MRI with a hybrid autoencoder framework can non-invasively infer TAMs burden in IDH-wildtype glioblastoma across heterogeneous cohorts. By combining representation learning, probabilistic calibration, and interpretability, DECIPHER-GBM extends radiomics toward a generalisable imaging biomarker framework. TAMs emerge as a stable and transferable immune phenotype under domain shift. Calibrated probabilistic outputs better capture uncertainty than binary framing, supporting scalable imaging-based immune stratification and future multimodal biomarker development.

References

1. Biggs, M.L., Wang, Y., Soni, N., Priya, S., Bathla, G., Canahuate, G.: Evaluating autoencoders for dimensionality reduction of MRI-derived radiomics and classification of malignant brain tumors. In: Proceedings of the 35th International Conference on Scientific and Statistical Database Management. SSDBM '23, ACM (2023). https://doi.org/10.1145/3603719.3603737

2. Calabrese, E., Rudie, J.D., Rauschecker, A.M., et al.: Combining radiomics and deep convolutional neural network features from preoperative MRI for predicting clinically relevant genetic biomarkers in glioblastoma. Neuro-Oncology Advances **4**, vdac060 (2022). https://doi.org/10.1093/noajnl/vdac060
3. Catani, G., Morchón-Araujo, D., Mirallas, O., et al.: Optimizing early-phase immunotherapy trials: The role of biomarker enrichment strategies. Frontiers in Immunology **16**, 1664443 (2025). https://doi.org/10.3389/fimmu.2025.1664443
4. Chang, L., Liu, J., Zhu, J., et al.: Advancing precision medicine: The transformative role of artificial intelligence in immunogenomics, radiomics, and pathomics for biomarker discovery and immunotherapy optimization. Cancer Biology & Medicine **22**, 33–47 (2025). https://doi.org/10.20892/j.issn.2095-3941.2024.0376
5. Chen, D., Zhang, R., Huang, X., et al.: MRI-derived radiomics assessing tumor-infiltrating macrophages enable prediction of immune-phenotype, immunotherapy response and survival in glioma. Biomarker Research **12**(1), 14 (2024). https://doi.org/10.1186/s40364-024-00560-6
6. Chen, J., Wu, Q., Berglund, A.E., et al.: Tumor-associated macrophages in glioblastoma: Mechanisms of tumor progression and therapeutic strategies. Cells **14**(18), 1458 (2025). https://doi.org/10.3390/cells14181458
7. Chen, S., Saeed, A.F.U.H., Liu, Q., et al.: Macrophages in immunoregulation and therapeutics. Signal Transduction and Targeted Therapy **8**(1), 207 (2023). https://doi.org/10.1038/s41392-023-01452-1
8. ClinicalTrials.gov: A multi-center, randomized, phase 2 trial of glioblastoma immunotherapy advancement with nivolumab and relatlimab (GIANT). https://clinicaltrials.gov/study/NCT06816927 (2025), clinicalTrials.gov Identifier: NCT06816927
9. Cloughesy, T.F., Mochizuki, A.Y., Orpilla, J.R., et al.: Neoadjuvant anti-PD-1 immunotherapy promotes a survival benefit with intratumoral and systemic immune responses in recurrent glioblastoma. Nature Medicine **25**(3), 477–486 (2019). https://doi.org/10.1038/s41591-018-0337-7
10. Eckert, T., Walton, C., Bell, M., et al.: The basis for targeting the tumor macrophage compartment in glioblastoma immunotherapy. Cancers (Basel) **17**(10), 1631 (2025). https://doi.org/10.3390/cancers17101631
11. Ghimire, P., Kinnersley, B., Karami, G., et al.: Radiogenomic biomarkers for immunotherapy in glioblastoma: A systematic review of magnetic resonance imaging studies. Neuro-Oncology Advances **6**, vdae055 (2024). https://doi.org/10.1093/noajnl/vdae055
12. Ghimire, P., Li, J., Yaou, L., et al.: Predictive radiomics for evaluation of cancer immune signature in glioblastoma: the precise-gbm study. Neuro-Oncology Advances **8**(1) (2026). https://doi.org/10.1093/noajnl/vdag115
13. Huang, R., Lu, X., Sun, X., Wu, H.: A novel immune cell signature for predicting glioblastoma after radiotherapy prognosis and guiding therapy. International Journal of Immunopathology and Pharmacology **38**, 3946320241249395 (2024). https://doi.org/10.1177/03946320241249395
14. Jia, D., Li, S., Li, D., et al.: Mining TCGA database for genes of prognostic value in glioblastoma microenvironment. Aging **10**(4), 592–605 (2018). https://doi.org/10.18632/aging.101415
15. Khalili, N., Kazerooni, A.F., et al.: Radiomics for characterization of the glioma immune microenvironment. npj Precision Oncology **7**, 59 (2023). https://doi.org/10.1038/s41698-023-00413-9

16. Klopfenstein, Q., Truntzer, C., Vincent, J., Ghiringhelli, F.: Cell lines and immune classification of glioblastoma define patient's prognosis. British Journal of Cancer **120**(8), 806–814 (2019). https://doi.org/10.1038/s41416-019-0404-y
17. Le Calvez, K., Mauricaite, R., Treasure, P., et al.: Adult glioblastoma in England: Incidence, treatment, and outcomes with novel population-based strata. Cancer Epidemiology **97**, 102811 (2025). https://doi.org/10.1016/j.canep.2025.102811
18. Li, D., Zhang, X., Du, Y.: Macrophage-based therapeutic strategies in glioblastoma: advancements in drug delivery and immunotherapy. Frontiers in Oncology **16**, 1746344 (2026). https://doi.org/10.3389/fonc.2026.1746344
19. Liu, D., Chen, J., Ge, H., et al.: Radiogenomics to characterize the immune-related prognostic signature associated with biological functions in glioblastoma. European Radiology **33**(1), 209–220 (2022). https://doi.org/10.1007/s00330-022-09012-x
20. Liu, X., Chen, H., Tan, G., et al.: A comprehensive neuroimaging review of the primary and metastatic brain tumors treated with immunotherapy: Current status, and the application of advanced imaging approaches and artificial intelligence. Frontiers in Immunology **15**, 1496627 (2024). https://doi.org/10.3389/fimmu.2024.1496627
21. Long, G.V., Shklovskaya, E., Satgunaseelan, L., et al.: Neoadjuvant triplet immune checkpoint blockade in newly diagnosed glioblastoma. Nature Medicine **31**(5), 1557–1566 (2025). https://doi.org/10.1038/s41591-025-03512-1
22. McFaline-Figueroa, J.R., Sun, L., Youssef, G.C., et al.: Neoadjuvant anti-PD1 immunotherapy for surgically accessible recurrent glioblastoma: Clinical and molecular outcomes of a stage 2 single-arm expansion cohort. Nature Communications **15**(1), 10757 (2024). https://doi.org/10.1038/s41467-024-54326-7
23. Pálsson, S., Cerri, S., Poulsen, H.S., et al.: Predicting survival of glioblastoma from automatic whole-brain and tumor segmentation of MR images. Scientific Reports **12**, 19744 (2022). https://doi.org/10.1038/s41598-022-19223-3
24. Sarfraz, Z., Ranjan, T., Mustafayev, F.N.A., et al.: Emerging therapies for glioblastoma. Journal of Neuro-Oncology **176**(1), 116 (2025). https://doi.org/10.1007/s11060-025-05248-x
25. Singh, G., Singh, A., Bae, J., et al.: New frontiers in domain-inspired radiomics and radiogenomics: Increasing role of molecular diagnostics in CNS tumor classification and grading following WHO CNS-5 updates. Cancer Imaging **24**, 133 (2024). https://doi.org/10.1186/s40644-024-00769-6
26. Song, P., Shen, C., Fan, Z., et al.: An integrated MRI-based diagnostic framework for glioma with incomplete imaging sequences and imperfect annotations. npj Precision Oncology **9**(1), 328 (2025). https://doi.org/10.1038/s41698-025-01112-3
27. Stupp, R., Mason, W.P., van den Bent, M.J., et al.: Radiotherapy plus concomitant and adjuvant temozolomide for glioblastoma. New England Journal of Medicine **352**(10), 987–996 (2005). https://doi.org/10.1056/NEJMoa043330
28. Xing, Z., Liu, Z., Fu, X., et al.: Clinical significance and immune landscape of a pyroptosis-derived LncRNA signature for glioblastoma. Frontiers in Cell and Developmental Biology **10**, 805291 (2022). https://doi.org/10.3389/fcell.2022.805291
29. Zhao, W., Zhang, Z., Xie, M., et al.: Exploring tumor-associated macrophages in glioblastoma: from diversity to therapy. npj Precision Oncology **9**(1), 126 (2025). https://doi.org/10.1038/s41698-025-00920-x